All-Epitaxial Resonant Cavity Enhanced Long-Wave Infrared Detectors for Focal Plane Arrays

P. Petluru,[1] A. J. Muhowski,[2] A. Kamboj,[1] N.C. Mansfield,[1] M. Bergthold,[1] E.A. Shaner,[2] J.F. Klem,[2] and D. Wasserman[1]

[1)]*University of Texas at Austin, Electrical and Computer Engineering, Austin, TX 78758, USA*

[2)]*Sandia National Laboratories, Albuquerque, New Mexico 87185, USA*

(*Electronic mail: dw@utexas.edu (Corresponding Author))

(Dated: 14 December 2022)

We demonstrate a monolithic all-epitaxial resonant-cavity architecture for long-wave infrared photodetectors with substrate-side-illumination. An nBn detector with an ultra-thin ($t \approx 350\,\text{nm}$) absorber layer is integrated into a leaky resonant cavity, formed using semi-transparent highly doped (n^{++}) epitaxial layers, and aligned to the anti-node of the cavity's standing wave. The devices are characterized electrically and optically, and demonstrate an external quantum efficiency of $\sim 25\%$ at $T = 180\,\text{K}$, in an architecture compatible with focal plane array configurations.

The mid-infrared (mid-IR, $2-20\,\mu\text{m}$) is a vital wavelength range for a number of sensing, security, and communication applications. Within the mid-IR, the atmospheric transmission window of the long-wave infrared (LWIR, $8-14\,\mu\text{m}$) is of particular interest as the spectral home to the peak black-body emission for temperatures between $\sim 200-350\,\text{K}$, as well as a large number of molecular absorption resonances, the latter earning the LWIR the moniker of the "spectral fingerprint region". For many of the various LWIR applications (free-space communication, gas sensing, thermal imaging)[1–4], efficient and high bandwidth ($\sim$ MHz) detection of LWIR light is required. The primary challenge for photon detection at LWIR wavelengths is that the low energy band-gap, which is required to absorb the low-frequency LWIR light, is also the source of significant dark current (I_{dark}), which has a linear dependence on the absorber thickness (t) and an exponential dependence on the band gap energy (E_g) and temperature (Eq. 1). The traditional metric for measuring mid-IR detector performance is the specific detectivity (D^*), which is a normalized signal (effectively the quantum efficiency, η) to noise ratio. The noise associated with a mid-IR detector, in diffusion-limited operation, is proportional to the square root of the dark current[5,6].

$$D^* \propto \frac{\eta}{\sqrt{I_{dark}}} \quad , \quad I_{dark} \propto t\, e^{-E_g/k_b T} \tag{1}$$

Because of the exponential increase in I_{dark} with decreasing band-gap (or increasing temperature), efficient room temperature detection in the LWIR has been a significant challenge.

The III-V semiconductors are a particularly appealing material system for LWIR detector development, due to the III-V's prominence in optoelectronics, significant fabrication infrastructure, and the design flexibility resulting from band structure engineering with III-V heterostructures. Such band structure engineering serves as the foundation for intersubband (ISB) LWIR detector architectures such as the quantum well, quantum dot, and quantum cascade infrared photodetectors (QWIP, QDIP, and QCD respectively)[7–10], as well as the interband cascade infrared photodetectors (ICIPs)[11]. The ISB and ICIP detectors offer extremely high bandwidth operation[7,12] due to fast ISB relaxation and inter-stage transit times[13], but suffer from weak absorption and, in the case of the QW-based detectors (QWIP, QCD), optical transition selection rules requiring in-coupling structures for normal incidence light[14]. There has also been significant interest in detectors utilizing type-II superlattices (T2SLs), comprising alternating layers of nm-scale thickness semiconductors with staggered or broken gap band alignment. For thin layers, electron and hole minibands form in the superlattice, with energy separation (effective band-gap) less than the band gap of either constituent material[15]. The T2SL offers significant wavelength flexibility and the integration of T2SL absorbers into a number of detector architectures such as p-i-n photodiodes[16] or alternatively, bariode (nBn or CBIRD) device architectures[17–19]. However, the nominal separation of electron and hole wavefunctions can result in substantially weaker absorption coefficients than in bulk IR-absorbing materials[20,21]. Thus much thicker T2SL absorber layers are required to achieve similar fractional absorption of incident light as bulk materials. Yet increasing absorber thickness provides diminishing returns, as a result of increasing dark current (Eq. 1) and decreasing carrier collection efficiency.

One potential approach to overcoming the low absorption coefficient of the T2SL is to engineer photonic structures capable of strongly confining incident light into small volumes, overlapping with detector active regions. This has been demonstrated using resonant cavities formed by epitaxially-grown Bragg reflectors beneath and above the detector[22], or with the top reflector replaced by Au[23]. Such approaches offer strong, narrow-band, MWIR detector response, but require extensive epitaxial growth. Extending epitaxial Bragg-reflector designs to the LWIR further increases the required device thickness (which scales with wavelength)[24]. Alternatively, detector active regions integrated with metallic gratings[25], or into metal-insulator-metal metamaterials[26], have shown significant enhancement in absorption, though the latter approach requires complex fabrication processes which could prove challenging when scaling to large area arrays. Recently, highly-doped (n^{++}) semiconductor layers have been monolithically integrated with IR detector active regions for enhanced external quantum efficiency (EQE) with ultra-thin

absorbers. The optical response of the n^{++} semiconductor can be modelled using the Drude formalism[27] and at high enough doping, can serve as a low index material (in the MWIR) or alternatively as a metallic, or even plasmonic, material in the LWIR. These materials have been integrated into guided-mode resonance detectors showing strongly enhanced MWIR response[28], and more recently, room-temperature operation[29]. At longer wavelengths, the doped semiconductor can serve as a reflecting back-plane in a leaky cavity configuration[30] or more recently, as a plasmonic material capable of supporting strongly confined optical modes overlapping with ultra-thin (≈ 300 nm) detector absorber layers[31]. The latter approach has been leveraged to demonstrate LWIR detector operation up to $T = 230$ K[32].

While thus far the demonstrations of LWIR detectors leveraging highly-doped (n^{++}) semiconductor materials have shown significant improvement in device performance (as measured by the specific detectivity, D^*), all used a surface (epi-side) illuminated configuration. While such surface-illuminated designs can be implemented in single-element LWIR detectors, much of the field of mid-IR detector development is motivated by the desire for high-operating-temperature (HOT) focal plane arrays (FPAs), which require substrate-side-illumination (SSI) for integration with read-out integrated circuitry (ROIC). Here we propose, demonstrate, and characterize a straightforward design for resonant cavity enhanced (RCE) LWIR response in a T2SL nBn detector. Our detector operates in SSI with strongly enhanced response at $\lambda \approx 10.8\ \mu m$. We demonstrate peak external quantum efficiencies of approximately 25% at $T = 180$ K in a device design fully compatible with FPA architectures.

Our detector was grown by molecular beam epitaxy on a lightly n-doped GaSb substrate in a Varian Gen-II system. The as-grown device stack is shown in Fig. 1a, and begins with a 466 nm thick highly doped n^{++} InAs/$InAs_{0.49}Sb_{0.51}$ T2SL layer, which acts as one mirror of the resonant cavity. This is followed by a 517 nm thick MWIR InAs/$InAs_{0.49}Sb_{0.51}$ T2SL layer with a period of 13.8 ML, and then a 346 nm thick LWIR InAs/$InAs_{0.49}Sb_{0.51}$ T2SL absorber layer, with a period of 34.3 ML. A 250 nm $AlAs_{0.1}Sb_{0.9}$ barrier is then grown on top of the LWIR absorber, followed by a 63 nm contact layer using the same T2SL as the LWIR absorber. The detector is designed to utilize a thin ($\ll \lambda_o$) LWIR absorber region to minimize dark current. Because the peak field amplitude, on resonance, is localized at the center of the cavity, LWIR absorber material outside of this region contributes little to responsivity, but significantly increases dark current. The MWIR spacer layer is designed to position the LWIR absorber in or near the peak field of the resonant cavity, minimize the barrier to electron transport, and because of its shorter cut-off wavelength, not contribute substantially to dark current. Likewise, the thick barrier layer was employed to position the LWIR absorber closer to the resonant field peak. Following growth, 200 µm × 200 µm mesas are etched through the detector stack, to the n^{++} layer, and 180 µm × 180 µm continuous metal contacts (Pd/Ti/Pt/Au) are deposited on the mesa top. Samples are mounted epi-down and the exposed GaSb substrate is not etched or coated.

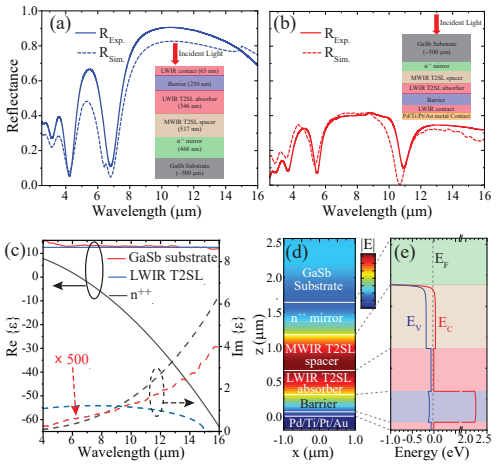

FIG. 1. Experimental (solid) and simulated (dashed) (a) front-side-illuminated reflectivity from the as-grown sample and (b) substrate-side illuminated reflectivity from the metal-coated device. Insets show the experimental configurations and layer stack for each measurement. (c) Complex permittivity of the GaSb substrate, n^{++} layer, and LWIR T2SL used in simulations. (d) On-resonance ($\lambda_o = 10.6$ µm) field profile for the substrate-side-illuminated structure. (e) Calculated band-structure of the epi-down sample.

The as-grown detector stack was characterized by x-ray diffraction and normal incidence epi-side-up infrared reflection spectroscopy (Fig. 1a, solid). A metal-coated sample was then characterized by normal incidence infrared reflection spectroscopy in a SSI configuration (Fig. 1b, solid). After epi-down mounting, the fabricated devices are placed in a temperature-controlled cryostat, and the detector's spectral response is measured using a Fourier transform spectrometer, and normalized to the response of a spectrally flat, calibrated detector. Responsivity is measured using a calibrated blackbody source and an 11.0 µm LWIR band-pass filter.

We model the optical properties of both the as-grown material, and the fabricated detectors, using rigorous coupled wave analysis (RCWA)[33]. The imaginary part of the MWIR and LWIR T2SL absorption is approximated by assuming an $\alpha = \alpha_0\sqrt{E - E_g}$ dependence for the absorption coefficient (where E_g is the T2SL bandgap) , with $E_{g,MWIR} = 5$ µm for the MWIR spacer layer, as calculated using the NextNano software package, and $E_{g,LWIR} = 15$ µm, extracted from experimental data. The magnitude of α_0 is calculated by fitting simulated to experimental EQE (taken both in front- and substrate-side illumination configurations). The real part of the permittivity for the T2SL layers and ternary barrier are calculated from a weighted average of their constituent binary materials. The n++ semiconductor is modeled as a Drude metal, with background permittivity $\varepsilon_b = 12.56$, plasma wavelength $\lambda_p = 6.5$ µm, and scattering rate $\gamma = 1x10^{13} rad/s$, ex-

tracted by fitting reflection spectra to the bare n^{++} layer. Figure 1a shows the simulated (dashed) reflectivity from the as-grown wafer for epi-up front side illumination. The SSI RCWA model assumes light incident from semi-infinite GaSb, with only the last 500 µm of GaSb modelled with loss. Modeled reflection (absorption) spectra are scaled twice (once) by the calculated reflection at the substrate/air interface, which removes the Fabry Perot fringes from the modeled spectra and more accurately reproduces the highly focused light of the experimental microscope reflection set-up. Both epi-up and SSI simulated reflection (Figs. 1a,b, dashed) accurately replicate the experimentally measured reflection.

A resonant absorption feature appears in the reflection spectra at $\lambda = 10.6\,\mu$m (Fig. 1b). The electric field distribution at this resonant wavelength is shown in Fig. 1d, and appears as would be expected for the fundamental resonant mode of the n^{++}/detector/contact metal cavity. Absorption in each layer can be found by calculating the difference in the integrated Poynting flux across the layer interfaces. For thin absorbers, we assume near-unity collection efficiency, such that the external quantum efficiency of the detector corresponds to the fractional absorption in the detector's absorber layer. This same approach also allows us to extract the loss in the n^{++} layer, which we simulate to be $\sim 15\%$ on resonance. We estimate the carrier density in this layer to be on the order of $5\times10^{19} cm^{-3}$. Simulation details can be found in previous work leveraging n^{++} layers for ultra-thin mid-IR detectors of varying architectures and across a range of wavelengths[28,29,31,32].

Figure 2 shows the experimental dark current density (and differential resistance dV/dI), as a function of applied bias, of the fabricated detector for a range of temperatures. Negative differential resistance is observed at biases of $\approx -2\,$V, a feature previously observed at turn-on in our ultra-thin detectors[32], and which is also observed to correlate with detector turn-on in the current detectors. The large turn-on voltage is coupled with a narrow dynamic range (in voltage and temperature) for optimal detector operation, pointing to a complicated interplay between a variety of device parameters, including various dark current mechanisms (G/R, Auger, and band-to-band tunneling) and the temperature dependence of the T2SL bandgap and band offsets. All of these would be problematic for most any detector application, but especially so for focal plane arrays (FPAs), where high operating voltages (and dark currents) are incompatible with FPA read-out integrated circuitry. However, the poor electrical characteristics of the device are not intrinsic to the detector architecture, nor are they central to this work, which is focused on the detector's resonant optical response. The modeled detector band structure, shown in Fig. 1e, clearly shows potential energy barriers to carrier transport at the LWIR/MWIR T2SL interface, and at the LWIR absorber/barrier interface, each of which could be addressed by optimizing band offsets between device layers. We have also observed high turn-on bias in detectors with thick barriers[28,31], which we attribute to unintentional doping of the wide band-gap barrier. Thinning the detector barrier can result in devices with turn on biases as low as $-100\,$mV[29]. At a device operating temperature of $T = 180\,$K,

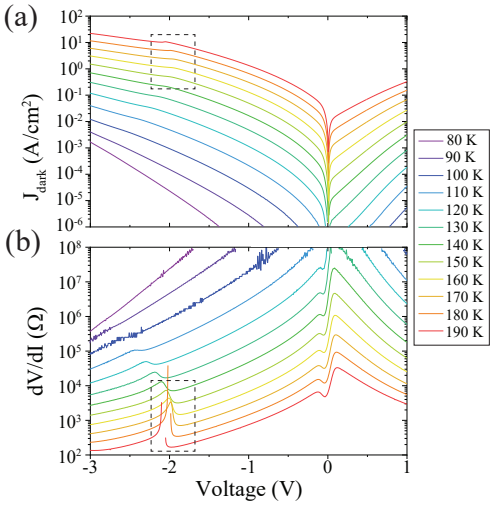

FIG. 2. Temperature-dependent (a) current density-voltage and (b) differential resistance dV/dI plots from $T = 80-190\,$K. The voltage range associated with the local differential resistance maximum (or negative differential resistance) at temperatures near the detector maximum operating temperature are highlighted by the dashed boxes.

our dark current density, at an operational bias of $V = -2.0\,$V, is $J_{dark} = 4.97\,\mathrm{A/cm^2}$, slightly above the dark current predicted by Rule 07[34], the long-used heuristic for state of the art HgCdTe photodetectors, and well above Law 19, which predicts the ultimate limit of HgCdTe dark currents absent Auger generation/recombination[35]. However, dark current associated with the large turn-on voltage in our device likely obscures the ultimate limit of dark current achievable in our detector architecture. Decreasing detector turn-on voltage could bring the detector dark current below Rule 07, as observed in previous ultra-thin detector architectures[31,32].

The measured external quantum efficiency of the epi-down detector, at $T = 180\,$K and $V = -2.0\,$V, is shown in Fig. 3 (solid, red) and compared to the simulated EQE (dashed,red). Because the metal contact of the fabricated device does not cover the entire mesa surface, we calculate the simulated EQE by weighting the modeled absorption for both bare and metal-coated bottom surfaces, proportional to the metal-coverage of the mesa (the un-coated mesa is predicted to have minimal absorption at resonance). The measured EQE is, in some ways, not entirely representative of the detector efficiency, as a commercial substrate-side illuminated LWIR detector would employ a thinned substrate (to minimize substrate absorption), and a coating on the thinned substrate to minimize reflection from the substrate-air interface. In Fig. 3 we include our simulated detector EQE in the absence of substrate absorption (green dashed), which is approximately 18% on resonance, measured from a bare GaSb wafer. Additionally, we

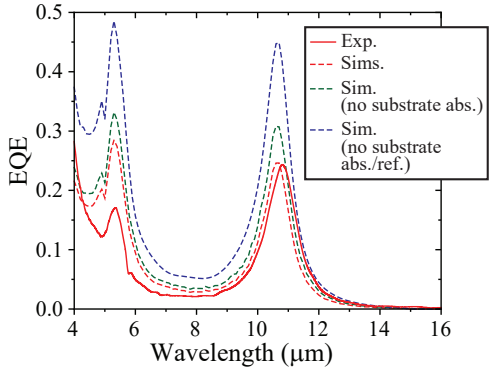

FIG. 3. Experimental (solid) and simulated (dashed) external quantum efficiency of a 200 μm × 200 μm mesa at $T = 180$ K. Simulated external quantum efficiency for ideal cases also shown: no substrate absorption (dashed green), no substrate absorption and no substrate/air reflection (dashed blue).

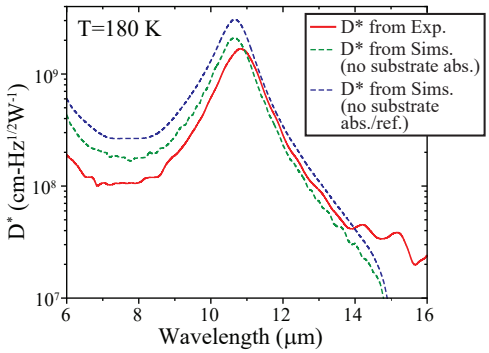

FIG. 4. Estimated specific detectivity as a function of wavelength at $T = 180$ K from experimental EQE (solid red), simulated EQE without substrate loss (green) and simulated EQE without substrate loss or substrate/air reflection (blue dashed).

include the simulated EQE in the absence of substrate absorption and assuming an ideal anti-reflective coating on the GaSb substrate (dashed blue). As can be seen in Fig. 3, the 'idealized' EQE could approach values as high as 45% on resonance, from an absorber only 346 nm thick ($\sim \lambda_o/30$).

Figure 4 shows the $T = 180$ K specific detectivity (D^*) of the resonant cavity enhanced detector. We estimate the specific detectivity with the expression:

$$D^* = R_i(\lambda)\sqrt{\frac{A}{2e|I| + 4k_bT/R}} \quad (2)$$

using the experimentally measured dark current (I) and responsivity ($R_i(\lambda)$), with mesa area A, Boltzmann's constant k_b, detector temperature T, and differential resistance R. The low dark current (a result of the thin LWIR absorber) and the significant EQE (on resonance) of our detector results in a peak detectivity of 1.68×10^9 $cm\sqrt{Hz}W^{-1}$, comparable with single-element, front-side-illuminated commercial LWIR detectors at similar temperatures[36]. There remain significant potential improvements to the performance of our resonant cavity enhanced detectors. A better overlap of the absorber with the peak electric field could improve peak EQE (and/or allow for even thinner absorbers with minimal degradation of EQE). Optimization of T2SL band alignment and barrier thickness would decrease turn-on voltage dramatically, which could significantly improve dark current. Increasing the LWIR absorber bandgap energy to be closer to, yet still below, the cavity resonance would also significantly reduce dark current. While the detector operating temperature and measured EQE are below those of previously demonstrated ultra-thin plasmonic LWIR detectors[31,32], the plasmonic detectors operate in an epi-up illumination configuration, and require surface patterning to couple into the plasmonic modes. Translating such structures to a SSI configuration is challenging (though not inconceivable), and requires either integrating a grating structure into the epitaxial growth[37], or bonding to a structured surface. Moreover, without any changes to the current device bandstructure and detector architecture, were substrate absorption and reflection to be minimized in our RCE design, peak specific detectivity could reach as high as 3.06×10^9 $cm\sqrt{Hz}W^{-1}$, as indicated in Fig. 4 (dashed blue).

In conclusion, we demonstrate a substrate-side illuminated, all-epitaxial resonant cavity-enhanced detector operating at 180K, showing an EQE of approximately 25% at $\lambda = 10.8$ μm. The peak field amplitude is designed to spatially overlap with the long-wave infrared absorber in an nBn detector integrated into the resonant cavity, allowing for strong absorption on resonance. Commercial detector fabrication techniques, such as substrate thinning and anti-reflection coating, could bring the EQE and specific detectivity of the current detector to 45% and 3.06×10^9 $cm\sqrt{Hz}W^{-1}$, respectively. Improvements to the device's optical design and band structure have the potential to dramatically reduce turn-on bias and dark current, and better align the absorber to the anti-node of the resonant mode, resulting in higher EQE and improved specific detectivity. This monolithic epitaxial device architecture, which leverages the optical and electronic co-design achievable with highly doped semiconductors and the 6.1 Å family of semiconductor alloys, is optically, geometrically, and (with improvements to device operating current and voltage) electrically compatible with focal plane array read-out circuitry, and thus offers a potential path towards the development of high operating temperature and high specific detectivity imaging arrays for long-wave infrared applications.

The data that support the findings of this study are available from the corresponding author upon reasonable request.

D.W. and P.P. gratefully acknowledge support from the National Science Foundation (No. ECCS-1926187). This work was partly done at the Texas Nanofabrication Facility, supported by NSF grant NNCI-2025227. This work was also

supported by the Laboratory Directed Research and Development program at Sandia National Laboratories, a multimission laboratory managed and operated by National Technology and Engineering Solutions of Sandia LLC, a wholly owned subsidiary of Honeywell International Inc. for the U.S. Department of Energy's National Nuclear Security Administration under contract DE-NA0003525. This article has been authored by an employee of National Technology & Engineering Solutions of Sandia, LLC under Contract No. DE-NA0003525 with the U.S. Department of Energy (DOE). The employee owns all right, title and interest in and to the article and is solely responsible for its contents. The United States Government retains and the publisher, by accepting the article for publication, acknowledges that the United States Government retains a non-exclusive, paid-up, irrevocable, worldwide license to publish or reproduce the published form of this article or allow others to do so, for United States Government purposes. The DOE will provide public access to these results of federally sponsored research in accordance with the DOE Public Access Plan https://www.energy.gov/downloads/doe-public-access-plan. This paper describes objective technical results and analysis. Any subjective views or opinions that might be expressed in the paper do not necessarily represent the views of the U.S. Department of Energy or the United States Government.

[1]X. Pang, O. Ozolins, S. Jia, L. Zhang, R. Schatz, A. Udalcovs, V. Bobrovs, H. Hu, T. Morioka, Y.-T. Sun, J. Chen, S. Lourdudoss, L. Oxenlowe, S. Popov, and X. Yu, "Bridging the terahertz gap: Photonics-assisted free-space communications from the submillimeter-wave to the mid-infrared," Journal of Lightwave Technology **40**, 3149–3162 (2022).

[2]J.-M. Melkonian, J. Armougom, M. Raybaut, J.-B. Dherbecourt, G. Gorju, N. Cezard, A. Godard, V. Pašiškevičius, R. Coetzee, and J. Kadlčák, "Long-wave infrared multi-wavelength optical source for standoff detection of chemical warfare agents," Applied Optics **59**, 11156–11166 (2020).

[3]R. Wood, *Infrared Detectors and Emitters: Materials and Devices; Edited by Peter Capper and C.T. Elliott*, Vol. 8 (Springer, 2001) pp. 149–175.

[4]N. García-Porta, F. J. Gantes-Nuñez, J. Tabernero, and S. Pardhan, "Characterization of the ocular surface temperature dynamics in glaucoma subjects using long-wave infrared thermal imaging," Journal of the Optical Society of America A **36**, 1015–1021 (2019).

[5]J. Piotrowski and W. Gawron, "Ultimate performance of infrared photodetectors and figure of merit of detector material," Infrared physics & technology **38**, 63–68 (1997).

[6]D. R. Rhiger, "Performance comparison of long-wavelength infrared type II superlattice devices with HgCdTe," Journal of Electronic Materials **40**, 1815–1822 (2011).

[7]B. Levine, "Quantum-well infrared photodetectors," Journal of Applied Physics **74**, R1–R81 (1993).

[8]K. W. Berryman, S. A. Lyon, and M. Segev, "Mid-infrared photoconductivity in InAs quantum dots," Applied Physics Letters **70**, 1861–1863 (1997).

[9]J. C. Campbell and A. Madhukar, "Quantum-dot infrared photodetectors," Proceedings of the IEEE **95**, 1815–1827 (2007).

[10]F. R. Giorgetta, E. Baumann, M. Graf, Q. Yang, C. Manz, K. Kohler, H. E. Beere, D. A. Ritchie, E. Linfield, A. G. Davies, Y. Fedoryshyn, H. Jackel, M. Fischer, J. Faist, and D. Hofstetter, "Quantum cascade detectors," IEEE Journal of Quantum Electronics **45**, 1039–1052 (2009).

[11]P. Martyniuk, A. Rogalski, and S. Krishna, "Interband quantum cascade infrared photodetectors: Current status and future trends," Physical Review Applied **17**, 027001–1–027001–36 (2022).

[12]D. Palaferri, Y. Todorov, A. Bigioli, A. Mottaghizadeh, D. Gacemi, A. Calabrese, A. Vasanelli, L. Li, A. G. Davies, E. H. Linfield, F. Kapsalidis, M. Beck, J. Faist, and C. Sirtori, "Room-temperature nine-m-wavelength photodetectors and GHz-frequency heterodyne receivers," Nature **556**, 85–88 (2018).

[13]H. Lotfi, L. Li, L. Lei, H. Ye, S. M. Shazzad Rassel, Y. Jiang, R. Q. Yang, T. D. Mishima, M. B. Santos, J. A. Gupta, and M. B. Johnson, "High-frequency operation of a mid-infrared interband cascade system at room temperature," Applied Physics Letters **108**, 201101 (2016).

[14]K. W. Goossen and S. A. Lyon, "Grating enhanced quantum well detector," Applied Physics Letters **47**, 1257–1259 (1985).

[15]D. L. Smith and C. Mailhiot, "Proposal for strained type II superlattice infrared detectors," J. Appl. Phys. **62**, 2545–2548 (1987).

[16]J. Schmidt, F. Rutz, V. Daumer, and R. Rehm, "Capacitance-voltage investigation of low residual carrier density in InAs/GaSb superlattice infrared detectors," Infrared Physics and Technology **84**, 3–6 (2017).

[17]P. Klipstein, "Xbn barrier photodetectors for high sensitivity and high operating temperature infrared sensors," in *Infrared Technology and Applications XXXIV*, Vol. 6940 (SPIE, 2008) pp. 935–946.

[18]S. Maimon and G. W. Wicks, "nbn detector, an infrared detector with reduced dark current and higher operating temperature," Applied Physics Letters **89**, 151109 (2006).

[19]D. Z.-Y. Ting, C. J. Hill, A. Soibel, S. A. Keo, J. M. Mumolo, J. Nguyen, and S. D. Gunapala, "A high-performance long wavelength superlattice complementary barrier infrared detector," Applied Physics Letters **95**, 023508 (2009).

[20]P. Webster, N. A. Riordan, S. Liu, E. H. Steenbergen, R. A. Synowicki, and Y.-H. Z. nd S. R. Johnson, "Absorption properties of type-II InAs/InAsSb superlattices measured by spectroscopic ellipsometry," Applied Physics Letters **106**, 061907 (2015).

[21]I. Vurgaftman, G. Belenky, Y. Lin, D. Donetsky, L. Shterengas, G. Kipshidze, W. L. Sarney, and S. P. Svensson, "Interband absorption strength in long-wave infrared type-II superlattices with small and large superlattice periods compared to bulk materials," Appl. Phys. Lett. **108**, 222101 (2016).

[22]V. Letka, A. Bainbridge, A. P. Craig, F. Al-Saymari, and A. R. J. Marshall, "Resonant cavity-enhanced photodetector incorporating a type-II superlattice to extend MWIR sensitivity," Opt. Express **27**, 23970–23980 (2019).

[23]C. L. Canedy, W. W. Bewley, C. D. Merritt, C. S. Kim, M. Kim, M. V. Warren, E. M. Jackson, J. A. Nolde, C. A. Affouda, E. H. Aifer, I. Vurgaftman, and J. R. Meyer, "Resonant-cavity infrared detector with five-quantum-well absorber and 34% external quantum efficiency at 4 m," Opt. Express **27**, 3771–3781 (2019).

[24]V. Letka, A. P. Craig, A. Bainbridge, and A. R. J. Marshall, "A superlattice-based resonant cavity enhanced photodetector operating in the long-wavelength infrared," Applied Physics Letters **117**, 073503–1–073503–5 (2020).

[25]J. A. Nolde, M. Kim, C. S. Kim, E. M. Jackson, C. T. Ellis, J. Abell, O. J. Glembocki, C. L. Canedy, J. G. Tischler, I. Vurgaftman, J. R. Meyer, and E. H. Aifer, "Resonant quantum efficiency enhancement of midwave infrared nbn photodetectors using one-dimensional plasmonic gratings," Applied Physics Letters **106**, 261109 (2015).

[26]M. D. Goldflam, E. A. Kadlec, B. V. Olson, J. F. Klem, S. D. Hawkins, S. Parameswaran, W. T. Coon, G. A. Keeler, T. R. Fortune, A. Tauke-Pedretti, J. R. Wendt, E. A. Shaner, P. S. Davids, J. K. Kim, and D. W. Peters, "Enhanced infrared detectors using resonant structures combined with thin type-II superlattice absorbers," Applied Physics Letters **109**, 251103 (2016).

[27]S. Law, D. C. Adams, A. M. Taylor, and D. Wasserman, "Mid-infrared designer metals," Opt. Express **20**, 12155 (2012).

[28]A. Kamboj, L. Nordin, P. Petluru, A. J. Muhowski, D. N. Woolf, and D. Wasserman, "All-epitaxial guided-mode resonance mid-wave infrared detectors," Applied Physics Letters **118**, 201102 (2021).

[29]A. Kamboj, L. Nordin, A. J. Muhowski, D. Woolf, and D. Wasserman, "Room-temperature mid-wave infrared guided-mode resonance detectors," IEEE Photonics Technology Letters **34**, 615–618 (2022).

[30]L. Nordin, A. Kamboj, P. Petluru, E. Shaner, and D. Wasserman, "All-epitaxial integration of long-wavelength infrared plasmonic materials and detectors for enhanced responsivity," ACS Photonics **7**, 1950–1956 (2020).

[31]L. Nordin, P. Petluru, A. Kamboj, A. J. Muhowski, and D. Wasserman, "Ultra-thin plasmonic detectors," Optica **8**, 1545–1551 (2021).

[32]L. Nordin, A. J. Muhowski, and D. Wasserman, "High operating temperature plasmonic infrared detectors," Applied Physics Letters **120**, 101103 (2022).

[33]V. Podolskiy, From V. A. Podolskiy's research group, see https://faculty.uml.edu//vpodolskiy/codes/index.html for a versatile

implementation of Rigorous Coupled Wave Analysis.

[34]W. E. Tennant, D. Lee, M. Zandian, E. Piquette, and M. Carmody, "MBE HgCdTe technology: A very general solution to IR detection, described by "rule 07", a very convenient heuristic," Journal of Electronic Materials **37** (2008).

[35]D. Lee, P. Dreiske, J. Ellsworth, R. Cottier, A. Chen, S. Tallaricao, A. Yulius, M. Carmody, E. Piquette, M. Zandian, and S. Douglas, "Law 19: The ultimate photodiode performance metric," International Society for Optics and Photonics (SPIE, 2020) pp. 93–105.

[36]V. System, See $https://vigo.com.pl/en/products_en/pcas-3te-12-0-1x0-1-to8-wznsear-70/$ for "Type II Superlattice Photoconductive Detector PCAS-3TE-12-0.10.1-TO8-wZnSeAR-70".

[37]A. M. Skipper, P. Petluru, D. J. Ironside, A. M. García, A. J. Muhowski, D. Wasserman, and S. R. Bank, "All-epitaxial, laterally structured plasmonic materials," Applied Physics Letters **120**, 161103 (2022).

Applied Physics Letters

PLEASE CITE THIS ARTICLE AS DOI: 10.1063/5.0131628

16 July 2024 00:11:03